



HAL
open science

Effective Potentials and Elastic Properties in the Lattice-Element Method: Isotropy and Transverse Isotropy

Hadrien Laubie, Siavash Monfared, Farhang Radjai, Roland J. M. Pellenq,
Franz-Josef Ulm

► **To cite this version:**

Hadrien Laubie, Siavash Monfared, Farhang Radjai, Roland J. M. Pellenq, Franz-Josef Ulm. Effective Potentials and Elastic Properties in the Lattice-Element Method: Isotropy and Transverse Isotropy. Journal of Nanomechanics and Micromechanics, 2017, 7 (3), pp.04017007. 10.1061/(ASCE)NM.2153-5477.0000125 . hal-02095033

HAL Id: hal-02095033

<https://hal.science/hal-02095033v1>

Submitted on 10 Apr 2019

HAL is a multi-disciplinary open access archive for the deposit and dissemination of scientific research documents, whether they are published or not. The documents may come from teaching and research institutions in France or abroad, or from public or private research centers.

L'archive ouverte pluridisciplinaire **HAL**, est destinée au dépôt et à la diffusion de documents scientifiques de niveau recherche, publiés ou non, émanant des établissements d'enseignement et de recherche français ou étrangers, des laboratoires publics ou privés.

Effective Potentials and Elastic Properties in the Lattice-Element Method: Isotropy and Transverse Isotropy

Hadrien Laubie¹; Siavash Monfared²; Farhang Radjai, Ph.D.³;
Roland Pellenq, Ph.D.⁴; and Franz-Josef Ulm, Ph.D.⁵

Abstract: Lattice approaches have emerged as a powerful tool to capture the effective mechanical behavior of heterogeneous materials using harmonic interactions inspired from beam-type stretch and rotational interactions between a discrete number of mass points. In this paper, the lattice element method (LEM) is reformulated within the conceptual framework of empirical force fields employed at the lattice scale. Within this framework, because classical harmonic formulations are but a Taylor expansion of nonharmonic potential expressions, they can be used to model both the linear and the nonlinear response of discretized material systems. Specifically, closed-form calibration procedures for such interaction potentials are derived for both the isotropic and the transverse isotropic elastic cases on cubic lattices, in the form of linear relations between effective elasticity properties and energy parameters that define the interactions. The relevance of the approach is shown by an application to the classical Griffith crack problem. In particular, it is shown that continuum-scale quantities of linear-elastic fracture mechanics, such as stress intensity factors (SIFs), are well captured by the method, which by its very discrete nature removes geometric discontinuities that provoke stress singularities in the continuum case. With its strengths and limitations thus defined, the proposed LEM is well suited for the study of multiphase materials whose microtextural information is obtained by, e.g., X-ray micro-computed tomography.

Introduction

Ever since its inception in the 1940s, lattice-type discretization and its algorithmic implementation, which can be generically called lattice element method (LEM), have been employed as a discrete representation of a solid (Hrennikoff 1941). This approach can alternatively be described as a discrete number of mass points interacting with a fixed number of neighboring mass points forming a regular or irregular lattice structure. Classically, interaction forces were derived by a mechanics analogy with truss (or spring) systems as central-force lattices in both two dimensions (2D) (Hansen et al. 1989; Topin et al. 2007) and three dimensions (3D) (Nayfeh and Hefzy 1978; Kostaske et al. 2012; Affes et al. 2012); but it was quickly recognized that such central-force lattices restrict the domain of application of the method to isotropic materials exhibiting a Poisson's ratio of $\nu = 1/3$ in 2D, and $\nu = 1/4$ in 3D, consistent

with the current understanding of the link between texture (here lattice) and the deformation behavior of materials (Greaves et al. 2011). In order to overcome this limitation, several authors suggested the addition of beam-type interactions between mass points in 2D (e.g., Schlangen and Garboczi 1996, 1997; Bolander and Saito 1998) and 3D with or without rotational degrees of freedom (Zhao et al. 2011), with up to 178 interactions for each node in the (random lattice) system (Lilliu et al. 1999; Lilliu and van Mier 2003). While the preceding approaches allowed removing some of the earlier limitations of the central-force model, a search of the relevant literature was not conclusive in finding a rational framework that clearly defines the different elements of the method, from the local interactions that link the lattice's mass points to the macroscopic properties of the assembly of links, which is, in short, the focus of this paper. Such a framework is needed though not only for elastic (i.e., reversible) phenomena, but also for extending the method to poroelasticity (Monfared et al. 2016) or dissipative phenomena, related to plastic deformation, fracture, and so on, for which the method is frequently applied (e.g., Affes et al. 2012; Bolander and Saito 1998; Hansen et al. 1989; Kostaske et al. 2012; Lilliu and van Mier 2003; Schlangen and Garboczi 1996, 1997; Topin et al. 2007; Zhao et al. 2011). To this end, a reformulation of LEM is proposed, much akin to potential of mean force approaches used in soft matter physics (e.g., Masoero et al. 2012; Ioannidou et al. 2016) where mass points, here belonging to a lattice structure, interact with their nearest neighbors through effective interaction potentials.

Lattice Element Method

Network

At the very foundation of lattice approaches is a discretization of matter by mass points connected by a finite number of links forming a lattice network. For purposes of simplification of the presentation, the focus here shall be on cubic lattices that are most suitable

¹Research Assistant, Dept. of Civil and Environmental Engineering, Massachusetts Institute of Technology, 77 Massachusetts Ave., Cambridge, MA 02139 (corresponding author). ORCID: <https://orcid.org/0000-0001-6420-5134>. E-mail: hlaubie@mit.edu

²Research Assistant, Dept. of Civil and Environmental Engineering, Massachusetts Institute of Technology, 77 Massachusetts Ave., Cambridge, MA 02139. E-mail: monfared@mit.edu

³Director of Research, Multiscale Material Science for Energy and Environment UMI 3466 CNRS-MIT, MIT Energy Initiative, Massachusetts Institute of Technology, Cambridge, MA 02139. E-mail: fradjai@mit.edu

⁴Director of Research, Multiscale Material Science for Energy and Environment UMI 3466 CNRS-MIT, MIT Energy Initiative, Massachusetts Institute of Technology, Cambridge, MA 02139. E-mail: pellenq@mit.edu

⁵Professor, Dept. of Civil and Environmental Engineering, Massachusetts Institute of Technology, 77 Massachusetts Ave., Cambridge, MA 02139. E-mail: ulm@mit.edu

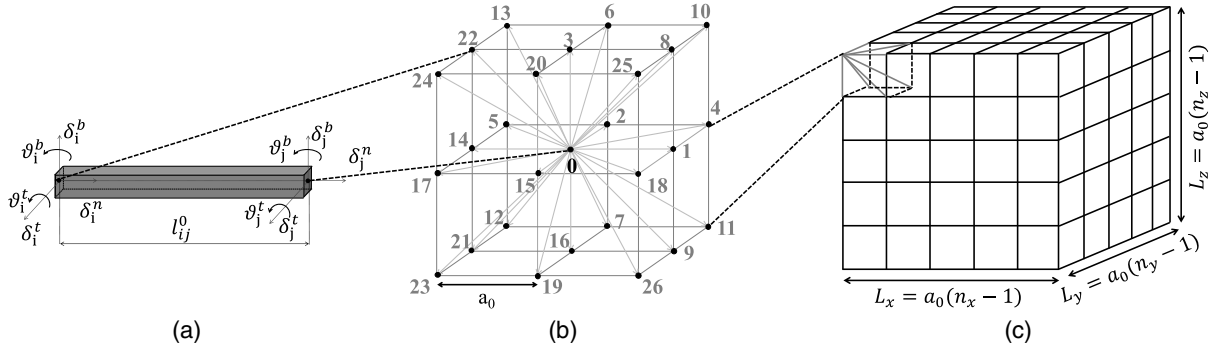


Fig. 1. (a) Degrees of freedom of the bond element joining nodes i and j ; (b) D3Q26 unit cell; (c) simulation box

Table 1. Length, Number, and Energy Parameters of the Different Links for the D3Q26 Lattice (13 Lines) and the D3Q18 Lattice (First 9 Lines)

Links $i - j$	Length l_{ij}^0	Number N_{ij}	Energy parameters isotropy	Transverse isotropy
0-1/0-14	a_0	$(n_x - 1)n_y n_z$	$\epsilon_1^{n,t}$	$\epsilon_1^{n,t}$
0-2/0-15	a_0	$n_x(n_y - 1)n_z$	$\epsilon_1^{n,t}$	$\epsilon_1^{n,t}$
0-3/0-16	a_0	$n_x n_y(n_z - 1)$	$\epsilon_1^{n,t}$	$\epsilon_3^t, \epsilon_1^t$
0-4/0-17	$\sqrt{2}a_0$	$(n_x - 1)(n_y - 1)n_z$	$\epsilon_4^{n,t}$	$\epsilon_4^{n,t}$
0-5/0-18	$\sqrt{2}a_0$	$(n_x - 1)(n_y - 1)n_z$	$\epsilon_4^{n,t}$	$\epsilon_4^{n,t}$
0-6/0-19	$\sqrt{2}a_0$	$n_x(n_y - 1)(n_z - 1)$	$\epsilon_4^{n,t}$	$\epsilon_6^t, \epsilon_4^t$
0-7/0-20	$\sqrt{2}a_0$	$n_x(n_y - 1)(n_z - 1)$	$\epsilon_4^{n,t}$	$\epsilon_6^t, \epsilon_4^t$
0-8/0-21	$\sqrt{2}a_0$	$(n_x - 1)n_y(n_z - 1)$	$\epsilon_4^{n,t}$	$\epsilon_6^t, \epsilon_4^t$
0-9/0-22	$\sqrt{2}a_0$	$(n_x - 1)n_y(n_z - 1)$	$\epsilon_4^{n,t}$	$\epsilon_6^t, \epsilon_4^t$
0-10/0-23	$\sqrt{3}a_0$	$(n_x - 1)(n_y - 1)(n_z - 1)$	$\epsilon_{10}^{n,t}$	$\epsilon_{10}^{n,t}$
0-11/0-24	$\sqrt{3}a_0$	$(n_x - 1)(n_y - 1)(n_z - 1)$	$\epsilon_{10}^{n,t}$	$\epsilon_{10}^{n,t}$
0-12/0-25	$\sqrt{3}a_0$	$(n_x - 1)(n_y - 1)(n_z - 1)$	$\epsilon_{10}^{n,t}$	$\epsilon_{10}^{n,t}$
0-13/0-26	$\sqrt{3}a_0$	$(n_x - 1)(n_y - 1)(n_z - 1)$	$\epsilon_{10}^{n,t}$	$\epsilon_{10}^{n,t}$

for the investigation of materials represented by voxels as obtained by 3D scans in, e.g., micro-computed tomography (Desrues et al. 2006). A typical example of such 3D cubic lattice systems are $D3Qn$ lattices, where D3 stands for the dimension and n for the number of links, as employed in lattice-Boltzmann simulations by the fluid transport community (e.g., D’Humières et al. 2002). For example, applied to solid systems, in D3Q18 (D3Q26) lattices, each mass point interacts with 18 (26) neighboring points, thus propagating forces and moments in 9 (13) directions. Given a unit cell (voxel) of size a_0 centered on Node 0, a D3Q18 lattice has six links of length $l^0 = a_0$, and 12 links of length $l^0 = \sqrt{2}a_0$, while a D3Q26 lattice has additional eight links of length $l^0 = \sqrt{3}a_0$ (Fig. 1). In such a cubic lattice, a solid domain is composed of $n_{x,y,z}$ mass points in the x, y, z direction defining unit cells. For such a geometry, the number N_{ij} of links of length $a_0, \sqrt{2}a_0$, and $\sqrt{3}a_0$ is given in Table 1.

Interaction Potentials

The effective interaction potential between two mass points i and j needs to be defined with respect to all possible translational and rotational degrees of freedom, δ_i and ϑ_i . Rotations are considered to be small ($|\vartheta_i| \ll 1$), so that classical vector rotation rules apply. The overriding constraints for setting up these potential expressions is that on the one hand, mass is conserved (that is automatically enforced by attributing the same mass to all points), and that on the other hand the forces and moments that derive from the

translational and rotational degrees of freedom between two mass points i and j satisfy equilibrium

$$\begin{aligned} \mathbf{F}_i^j &= -\frac{\partial U_{ij}}{\partial \delta_i}; & \mathbf{F}_i^j + \mathbf{F}_j^i &= \mathbf{0} \\ \mathbf{M}_i^j &= -\frac{\partial U_{ij}}{\partial \vartheta_i}; & \mathbf{M}_i^j + \mathbf{M}_j^i + \mathbf{r}_{ij} \times \mathbf{F}_j^i &= \mathbf{0} \end{aligned} \quad (1)$$

where $\mathbf{r}_{ij} = l_{ij}^0 \mathbf{e}_n$ = vector connecting node i to node j of rest-length l_{ij}^0 and oriented by the unit vector \mathbf{e}_n in a local orthonormal basis ($\mathbf{e}_n, \mathbf{e}_b, \mathbf{e}_t$) [see Appendix I for the transformation from the global system of coordinates ($\mathbf{e}_x, \mathbf{e}_y, \mathbf{e}_z$) to the local one]. The most general deformation arguments of any effective potential U_{ij} that defines the interactions between two mass points i and j while satisfying the Newton constraints [Eq. (1)] are

$$U_{ij} = U_{ij}(\mathbf{x}_j - \mathbf{x}_i = \delta_j - \delta_i + \mathbf{r}_{ij} \times \vartheta_i; \vartheta_j - \vartheta_i) \quad (2)$$

where \mathbf{x}_i = position vectors of mass point i in the deformed configuration.

Given this general form, one can separate the interaction energy terms between two mass points into two distinct contributions, $U_{ij} = U_{ij}^s + U_{ij}^b$: one related to two-body interactions, $U_{ij}^s = U_{ij}^s[(\mathbf{x}_j - \mathbf{x}_i) \cdot \mathbf{e}_n = \delta_j^n - \delta_i^n]$; the other associated to rotations (which relate to three-body interactions at the particle scale) $U_{ij}^b = U_{ij}^b[(\mathbf{x}_j - \mathbf{x}_i) \cdot \mathbf{e}_b; (\mathbf{x}_j - \mathbf{x}_i) \cdot \mathbf{e}_t; \vartheta_j - \vartheta_i]$, where $(\mathbf{x}_j - \mathbf{x}_i) \cdot \mathbf{e}_b = \delta_j^b - \delta_i^b - l_{ij}^0 \vartheta_i^b$ and $(\mathbf{x}_j - \mathbf{x}_i) \cdot \mathbf{e}_t = \delta_j^t - \delta_i^t + l_{ij}^0 \vartheta_i^t$. The coupling between translational and rotational degrees of freedom are

noteworthy in the arguments of the three-body interaction energy, which is of some importance when adopting nonharmonic potential expressions for the two-body interactions, and harmonic approximations for the three-body interactions, as frequently employed in, e.g., molecular simulations (e.g., [Falk et al. 2015](#)). That is, the general form of the interaction potential here derived allows accommodating a large range of possible effective potential expressions.

By way of example, consider first harmonic expressions motivated by truss-beam theory, currently in use in lattice element simulations and introduced by [Schlangen and Garboczi \(1996\)](#) for the two-dimensional case. An effective potential consistent with the truss-beam model has the following expression for the two-body interaction:

$$U_{ij}^s = \frac{1}{2} \epsilon_{ij}^n \left(\frac{\delta_j^n - \delta_i^n}{l_{ij}^0} \right)^2 \quad (3)$$

and for the three-body-bending interaction, neglecting torsional terms, while considering a quadratic development of its arguments

$$\begin{aligned} U_{ij}^b = \frac{1}{2} \epsilon_{ij}^t \left\{ \left(\frac{\delta_j^b - \delta_i^b}{l_{ij}^0} - \vartheta_i^t \right)^2 + \left(\frac{\delta_j^t - \delta_i^t}{l_{ij}^0} + \vartheta_i^b \right)^2 \right. \\ \left. + \left(\frac{\delta_j^b - \delta_i^b}{l_{ij}^0} - \vartheta_i^t \right) (\vartheta_i^t - \vartheta_j^t) + \left(\frac{\delta_j^t - \delta_i^t}{l_{ij}^0} + \vartheta_i^b \right) (\vartheta_j^b - \vartheta_i^b) \right. \\ \left. + \frac{1}{3} [(\vartheta_j^b - \vartheta_i^b)^2 + (\vartheta_i^t - \vartheta_j^t)^2] \right\} \quad (4) \end{aligned}$$

with $\epsilon_{ij}^{n,t} \geq 0$ being the normal and transverse energy parameters governing the elastic two-body and three-body interaction, respectively. These energy parameters must be positive in order to guarantee the convexity of the energy function. Negative values could make the reference configuration unstable. In classical Navier-Bernoulli beam theory, $\epsilon_{ij}^n = EA l_{ij}^0$ and $\epsilon_{ij}^t = 12EI/l_{ij}^0$, with E being the Young's modulus, A being the beam section, and I being the second-order area moment. However, when adopting a harmonic potential expression for an effective potential to describe a solid's behavior, the energies $\epsilon_{ij}^{n,t}$ remain to be determined with respect to the three-dimensional elastic behavior of the solid. This will be shown subsequently. In its turn, application of Eqs. (3) and (4) in the force and moment expressions in Eq. (1) provides for the harmonic case

$$\begin{aligned} \mathbf{F}_i^j = -\frac{\partial U_{ij}}{\partial \mathbf{\delta}_i} = \underbrace{\frac{\epsilon_{ij}^n}{l_{ij}^0} \left(\frac{\delta_j^n - \delta_i^n}{l_{ij}^0} \right) \mathbf{e}_n}_{\mathbf{F}_i^{j,n}} + \underbrace{\frac{\epsilon_{ij}^t}{l_{ij}^0} \left[\frac{\delta_j^b - \delta_i^b}{l_{ij}^0} - \frac{1}{2} (\vartheta_j^t + \vartheta_i^t) \right] \mathbf{e}_b}_{\mathbf{F}_i^{j,b}} \\ + \underbrace{\frac{\epsilon_{ij}^t}{l_{ij}^0} \left[\frac{\delta_j^t - \delta_i^t}{l_{ij}^0} + \frac{1}{2} (\vartheta_j^b + \vartheta_i^b) \right] \mathbf{e}_t}_{\mathbf{F}_i^{j,t}} \quad (5) \end{aligned}$$

and

$$\begin{aligned} \mathbf{M}_i^j = -\frac{\partial U_{ij}}{\partial \mathbf{\theta}_i} = \underbrace{\frac{\epsilon_{ij}^t}{2} \left[\frac{\delta_j^t - \delta_i^t}{l_{ij}^0} + \frac{1}{3} (\vartheta_j^b + 2\vartheta_i^b) \right] \mathbf{e}_b}_{\mathbf{M}_i^{j,b}} \\ + \underbrace{\frac{\epsilon_{ij}^t}{2} \left[\frac{\delta_j^b - \delta_i^b}{l_{ij}^0} - \frac{1}{3} (\vartheta_j^t + 2\vartheta_i^t) \right] \mathbf{e}_t}_{\mathbf{M}_i^{j,t}} \quad (6) \end{aligned}$$

As a second example a Mie (generalized Lennard-Jones) (MLJ) effective potential ([Avenidaño et al. 2011](#)) is considered, as was suggested in [van Mier \(2007\)](#). This classical nonharmonic potential for two-body interactions takes the form

$$\begin{aligned} U_{ij}^{\text{MLJ},s} &= \frac{\epsilon_{ij}^{\text{MLJ},n}}{\gamma - 1} \gamma^{[\gamma/(\gamma-1)]} \left[\left(\frac{\sigma}{r_{ij}} \right)^{\gamma\alpha} - \left(\frac{\sigma}{r_{ij}} \right)^\alpha \right] \\ &= \frac{\epsilon_{ij}^{\text{MLJ},n}}{\gamma - 1} \left[\left(1 + \frac{\delta_j^n - \delta_i^n}{l_{ij}^0} \right)^{-\gamma\alpha} - \gamma \left(1 + \frac{\delta_j^n - \delta_i^n}{l_{ij}^0} \right)^{-\alpha} \right] \quad (7) \end{aligned}$$

where $\epsilon_{ij}^{\text{MLJ},n}$ = depth of the potential well; $r_{ij} = l_{ij}^0 + \delta_j^n - \delta_i^n$ = normal distance between the two mass points; $\sigma = l_{ij}^0 \gamma^{1/[\alpha(1-\gamma)]}$ = distance between the two mass points at which the potential is zero; while the $r_{ij}^{-\alpha}$ term defines the short-range repulsion (in compression), and the $r_{ij}^{-\alpha}$ term defines the long-range attraction (in tension). A Taylor expansion of the MLJ potential around the equilibrium state [$\Delta = (\delta_j^n - \delta_i^n)/l_{ij}^0 \rightarrow 0$] reads

$$U_{ij}^{\text{MLJ},s} = \epsilon_{ij}^{\text{MLJ},n} \left[-1 + \frac{\gamma\alpha^2}{2} \Delta^2 + O(\Delta^3) \right] \quad (8)$$

and shows that the harmonic energy parameter ϵ_{ij}^n and the MLJ energy parameter $\epsilon_{ij}^{\text{MLJ},n}$ are related by

$$\epsilon_{ij}^{\text{MLJ},n} = \frac{1}{\gamma\alpha^2} \epsilon_{ij}^n \quad (9)$$

Otherwise said, the harmonic approximation around the equilibrium state can be used as a means of calibration of the nonharmonic potential; here the Mie-Lennard-Jones potential. Considering the order of the rotations is small (and neglecting nonlinear phenomena such as buckling), it is generally sufficient to employ nonharmonic potentials only for the two-body interactions, while considering harmonic expressions for the three-body and rotational interactions. Thus, compared to the harmonic case [Eq. (5)], only the central-force $F_i^{j,n}$ is modified, reading in the MLJ case

$$\begin{aligned} F_i^{j,n} = \mathbf{F}_i^j \cdot \mathbf{e}_n = \frac{\epsilon_{ij}^{\text{MLJ},n}}{l_{ij}^0} \frac{\gamma\alpha}{1-\gamma} \left[\left(1 + \frac{\delta_j^n - \delta_i^n}{l_{ij}^0} \right)^{-(\gamma\alpha+1)} \right. \\ \left. - \left(1 + \frac{\delta_j^n - \delta_i^n}{l_{ij}^0} \right)^{-(\alpha+1)} \right] \quad (10) \end{aligned}$$

While the choice of both displacement and rotational degrees of freedom gives rise to forces and moments, only the forces enter the virial expression ([Christoffersen et al. 1981](#)) to calculate the stress tensor at mass point i ; that is, neglecting the momentum terms and making use of the action reaction law in Eq. (1)

$$\boldsymbol{\sigma}_i = \frac{1}{V_i} \sum_{j=1}^{N_i^b} \mathbf{r}_{ij} \otimes \mathbf{F}_i^j \quad (11)$$

with $V_i = a_0^3$ is the volume of the unit cell; and N_i^b = number of node i 's neighboring mass points. In return, due to Eq. (1), the (bending) moments associated with the rotational degrees of freedom ensure moment equilibrium. It is this moment equilibrium that ensures the symmetry of the stress tensor. To show this, recall that the sum of all external moments acting on node i must vanish; that is, in terms of Eq. (1)

$$\mathbf{0} = \sum_{j=1}^{N_i^b} \mathbf{r}_{ij} \times \mathbf{F}_i^j = \sum_{j=1}^{N_i^b} \sum_{k=1}^3 [(\mathbf{r}_{ij} \times \mathbf{F}_i^j) \cdot \mathbf{e}_k] \mathbf{e}_k \quad (12)$$

$$C_{ijkl} = \frac{1}{V} \frac{\partial^2 \bar{U}_{\text{tot}}}{\partial \varepsilon_{ij} \partial \varepsilon_{kl}} \quad (17)$$

Then, use the relation between the cross and tensorial products of two vectors, $(\mathbf{a} \times \mathbf{b}) \cdot \mathbf{e}_k = \mathbf{e}_k' \cdot (\mathbf{a} \otimes \mathbf{b} - \mathbf{b} \otimes \mathbf{a}) \cdot \mathbf{e}_k''$ with $(\mathbf{e}_k, \mathbf{e}_k', \mathbf{e}_k'')$ a right-handed orthonormal basis. The moment equilibrium can thus be developed in the form

$$\mathbf{0} = \sum_{j=1}^{N_i^b} \sum_{k=1}^3 [\mathbf{e}_k' \cdot (\mathbf{r}_{ij} \otimes \mathbf{F}_i^j - \mathbf{F}_i^j \otimes \mathbf{r}_{ij}) \cdot \mathbf{e}_k''] \mathbf{e}_k \quad (13a)$$

$$= \sum_{k=1}^3 V_i [\mathbf{e}_k' \cdot (\boldsymbol{\sigma}_i - {}^T \boldsymbol{\sigma}_i) \cdot \mathbf{e}_k''] \mathbf{e}_k \quad (13b)$$

where the definition, Eq. (11), of the virial stress at node i , $\boldsymbol{\sigma}_i$, is used. This shows that satisfying the moment equilibrium ensures the symmetry of the stress tensor $\mathbf{e}_k' \cdot (\boldsymbol{\sigma}_i - {}^T \boldsymbol{\sigma}_i) \cdot \mathbf{e}_k'' = 0$ for all $k \in \{1, 2, 3\}$; that is, $\boldsymbol{\sigma}_i = {}^T \boldsymbol{\sigma}_i$. With a view on the energy expression in Eq. (4), this underscores the importance of considering rotational degrees of freedom, $\boldsymbol{\vartheta}_j$, when $\varepsilon_{ij}^t \neq 0$, to ensure the symmetry of the stress tensor.

Effective Elastic Properties

The use of the energy formulation permits a straightforward determination of the effective elastic properties of a macroscopic assembly of links in function of the unit cell's properties. To simplify the presentation, the focus here is on 3D-cubic lattices ($n_x = n_y = n_z = n$) and quasi-2D lattices ($n_x = n_z = n, n_y = 2$). Starting point is the total energy of the lattice as a sum of the energy of all links defined by Eq. (2)

$$U_{\text{tot}} = \sum_{\text{links } ij} U_{ij}(\boldsymbol{\delta}_j - \boldsymbol{\delta}_i + \mathbf{r}_{ij} \times \boldsymbol{\vartheta}_i; \boldsymbol{\vartheta}_j - \boldsymbol{\vartheta}_i) \quad (14)$$

For the calculation of the elastic constants, C_{ijkl} , around the (thermodynamic) equilibrium situation, it suffices to consider a uniform deformation field, for which the total energy is conveniently rewritten as

$$U_{\text{tot}} = \sum_{i=1}^{9(13)} N_{0i} U_{0i}(\boldsymbol{\delta}_i - \boldsymbol{\delta}_0 + \mathbf{r}_{0i} \times \boldsymbol{\vartheta}_i) \quad (15)$$

where the summation is carried out over the 9 (13) links directions of the D3Q18 (D3Q26) lattice. Expressions for N_{0i} are given in Table 1. It then suffices to express the arguments of the energy U_{0i} in terms of strains and rotations

$$\begin{aligned} \delta_i^{n,b,t} - \delta_0^{n,b,t} &= l_{0i}^0 \boldsymbol{\Delta}_{ji}^{n,b,t} \varepsilon_j \\ \vartheta_i^{b,t} &= \mathbf{P}_{ji}^{b,t} \theta_j \end{aligned} \quad (16)$$

where Einstein's summation rule is employed. Herein, ε_j = strain components $\{\varepsilon\} = (\varepsilon_{xx}, \varepsilon_{yy}, \varepsilon_{zz}, \varepsilon_{yz}, \varepsilon_{xz}, \varepsilon_{xy})$, and $\{\theta\} = (\vartheta_x, \vartheta_y, \vartheta_z)$, the rotational degrees of freedom in the global system of coordinates, while $\boldsymbol{\Delta}^{n,b,t}$ and $\mathbf{P}^{b,t}$ are transformation matrices whose expression are given in Appendix I. The use of Eq. (16) in Eq. (15) provides an expression of the total energy in function of $\{\varepsilon\}$ and $\{\theta\}$, i.e., $U_{\text{tot}}(\{\varepsilon\}, \{\theta\})$, which can be readily employed to derive the elastic stiffness of the lattice from

where $V = (n_x - 1)(n_y - 1)(n_z - 1)a_0^3$ = total volume. Furthermore, the energy $\bar{U}_{\text{tot}}(\{\varepsilon\}) = \min_{\{\theta\}} U_{\text{tot}}(\{\varepsilon\}, \{\theta\})$ evokes the theorem of minimum potential energy, which is generally valid for any harmonic potential expression. It also holds for nonharmonic potentials around the equilibrium state. As will be shown subsequently, the framework here defined permits an effective means to calibrate the energy parameters that define the interaction potentials.

From Cubic Symmetry to Isotropy

Consider first the case of isotropic materials that are fully characterized by two elastic constants; for instance, the stiffness constants $C_{11} = C_{1111}$ and $C_{13} = C_{1133}$ (in Voigt notation). The other nonzero stiffness constants satisfy $C_{11} = C_{22} = C_{33}$, $C_{12} = C_{13} = C_{23}$, and $C_{44} = C_{55} = C_{66} = (C_{11} - C_{12})/2$. Because the same properties must be observed in all directions, an effective isotropic behavior requires 4 (6) energy parameters $\varepsilon_{1,4(10)}^{n,t}$ for the D3Q18 (D3Q26) lattice (Table 1). It is thus convenient to rewrite the elastic stiffness tensor in Eq. (17) in a linear form of the energy parameters

$$C_i = \mathbf{A}_{ij}^{Iso} \varepsilon_j \quad (18)$$

where $\{C\} = (C_{11}, C_{13}, C_{55})$, and $\{\varepsilon\} = (\varepsilon_1^n, \varepsilon_4^n, \varepsilon_{10}^n, \varepsilon_1^t, \varepsilon_4^t, \varepsilon_{10}^t)$. The linear operator \mathbf{A}^{Iso} depends on the type of lattice, and—for finite size domains—on the size n of the simulation box. For instance, for the 3D-cubic lattice ($n_x = n_y = n_z = n$), it reads

$$\mathbf{A}^{Iso,3D} = \frac{1}{a_0^3} \begin{bmatrix} \frac{n^2}{(n-1)^2} & \frac{n}{n-1} & \frac{4}{9} & 0 & \frac{n}{n-1} & \frac{8}{9} \\ 0 & \frac{n}{2(n-1)} & \frac{4}{9} & 0 & -\frac{n}{2(n-1)} & -\frac{4}{9} \\ 0 & \frac{n}{2(n-1)} & \frac{4}{9} & \frac{n^2}{2(n-1)^2} & \frac{n}{2(n-1)} & \frac{2}{9} \end{bmatrix} \quad (19)$$

and for the quasi-2D lattices ($n_x = n_z = n, n_y = 2$)

$$\mathbf{A}^{Iso,2D} = \frac{1}{a_0^3} \begin{bmatrix} \frac{2n}{n-1} & \frac{3n-2}{2(n-1)} & \frac{4}{9} & 0 & \frac{3n-2}{2(n-1)} & \frac{8}{9} \\ 0 & 1 & \frac{4}{9} & 0 & -1 & -\frac{4}{9} \\ 0 & 1 & \frac{4}{9} & \frac{n}{n-1} & \frac{n}{2(n-1)} & \frac{2}{9} \end{bmatrix} \quad (20)$$

From these linear expressions, one readily recognizes the classical features of the central-force lattice model, which is obtained by letting $\varepsilon_i^t = 0$. In fact, in this case, the Cauchy condition is recovered, $C_{13} = C_{55}$, as well known from crystal chemistry: “for a primitive cubic solid in equilibrium at zero applied stress under the action of central, pairwise forces only, the elastic constants satisfy the Cauchy condition” (Thomas 1971). Moreover, the lattice symmetries naturally induce cubic symmetries (three independent stiffness constants instead of two).

The application of such cubic lattices to isotropic material systems thus requires one additional constraint on the energy constants $\varepsilon_i^{n,t}$ to ensure the isotropic relation

$$G = C_{55} = \frac{C_{11} - C_{13}}{2} = \frac{E}{2(1 + \nu)} \quad (21)$$

where G = shear modulus; E = Young's modulus; and ν = Poisson's ratio. In the case of the central-force lattice model ($\epsilon_i^t = 0$), Eq. (21) together with the Cauchy condition, $C_{13} = C_{55} = G$, implies $C_{11} = 3G$, which defines the well-known restriction of the model to a single value of the Poisson's ratio; namely, $\nu^{3D} = C_{13}/(C_{11} + C_{13}) = 1/4$ for the 3D-cubic lattice, and $\nu^{2D} = C_{13}/C_{11} = 1/3$ for the quasi-2D lattice. That is, rotational degrees of freedom associated with nonzero values for ϵ_i^t are required to capture a larger range of isotropic elastic materials. Keeping in mind that the energy parameters must be positive ($\epsilon_i^{n,t} \geq 0$), the isotropic constraint in Eq. (21) defines a limited range for possible values of the Poisson's ratio that can be captured with specific lattice systems. For instance, for the considered D3Q18 and D3Q26 lattices, Eqs. (19) and (20) give

$$-1 < \nu^{3D} \leq 1/4 \quad -2/3 \leq \nu^{2D} \leq 1/3 \quad (22)$$

While values outside of this range could be theoretically obtained by considering negative values of the energy parameters, such negative values may entail instabilities of the energy minimization that defines the equilibrium state.

It is thus possible to employ the approach in an inverse approach for the calibration of the harmonic interaction potential parameters for a given set of (effective) elastic properties by solving the linear

system of Eq. (18), while respecting the isotropic constraint relation in Eq. (21). Specifically, within the limits thus defined by Eq. (22), a minimum of three nonzero energy parameters $\epsilon_i^{n,t} \geq 0$ and a minimum of 18 directions are required to properly model an isotropic behavior for harmonic potentials. As noted previously, this calibration still holds for nonharmonic potentials when considering the harmonic case as a Taylor expansion of the nonharmonic case around the equilibrium state, i.e., Eq. (9). Diagonal links are of critical importance to reproduce the Poisson contraction. Table 2 provides a sample choice for these parameters $\epsilon_i^{n,t}$ in function of the two elastic parameters E and ν .

Transverse Isotropy

Using the same formalism, anisotropic materials can be modeled with LEM. By way of example, consider transversely isotropic materials, i.e., materials that exhibit rotational symmetry around an axis (say $\mathbf{e}_3 = \mathbf{e}_z$) normal to a plane of isotropy: $C_{11} = C_{22}$, $C_{13} = C_{23}$, and $C_{44} = C_{55}$. Particular symmetries were chosen (Table 1) so that the effective stiffness constants are linear functions of the energy parameters

$$C_i = \mathbf{A}_{ij}^{TI} \epsilon_j \quad (23)$$

where $\{C\} = [C_{11}(\cdot), C_{12}, C_{13}, C_{33}, C_{55}(\cdot), C_{66}]$ in 2D (3D), $\{\epsilon\} = (\epsilon_1^n, \epsilon_3^n, \epsilon_4^n, \epsilon_6^n, \epsilon_{10}^n, \epsilon_1^t, \epsilon_4^t, \epsilon_{10}^t)$. The linear operator \mathbf{A}_{ij}^{TI} for the 3D lattice is defined by

$$\mathbf{A}^{TI,3D} = \frac{1}{a_0^3} \begin{bmatrix} \frac{n^2}{(n-1)^2} & 0 & \frac{n}{2(n-1)} & \frac{n}{2(n-1)} & \frac{4}{9} & 0 & \frac{n}{n-1} & \frac{8}{9} \\ 0 & 0 & \frac{n}{2(n-1)} & 0 & \frac{4}{9} & 0 & -\frac{n}{2(n-1)} & -\frac{4}{9} \\ 0 & 0 & 0 & \frac{n}{2(n-1)} & \frac{4}{9} & 0 & -\frac{n}{2(n-1)} & -\frac{4}{9} \\ 0 & \frac{n^2}{(n-1)^2} & 0 & \frac{n}{n-1} & \frac{4}{9} & 0 & \frac{n}{n-1} & \frac{8}{9} \\ 0 & 0 & 0 & \frac{n}{2(n-1)} & \frac{4}{9} & \frac{n^2}{2(n-1)^2} & \frac{n}{2(n-1)} & \frac{2}{9} \\ 0 & 0 & \frac{n}{2(n-1)} & 0 & \frac{4}{9} & \frac{n^2}{2(n-1)^2} & \frac{n}{2(n-1)} & \frac{2}{9} \end{bmatrix} \quad (24)$$

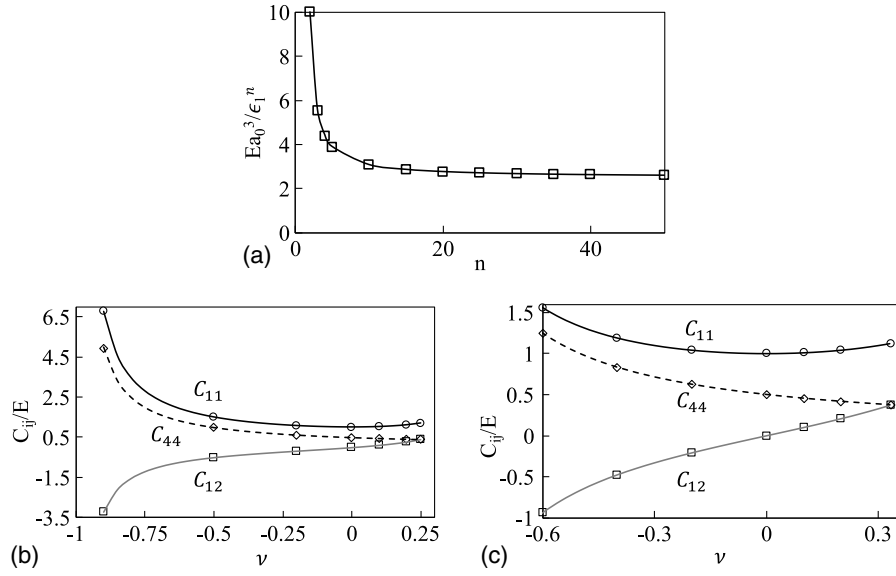
and for the 2D lattice it is defined by

$$\mathbf{A}^{TI,2D} = \frac{1}{a_0^3} \begin{bmatrix} \frac{2n}{n-1} & 0 & \frac{n}{2(n-1)} & 1 & \frac{4}{9} & 0 & \frac{3n-2}{2n-2} & \frac{8}{9} \\ 0 & 0 & 0 & 1 & \frac{4}{9} & 0 & -1 & -\frac{4}{9} \\ 0 & \frac{2n}{n-1} & 0 & \frac{3n-2}{2(n-1)} & \frac{4}{9} & 0 & \frac{3n-2}{2(n-1)} & \frac{8}{9} \\ 0 & 0 & 0 & 1 & \frac{4}{9} & \frac{n}{n-1} & \frac{n}{2(n-1)} & \frac{2}{9} \end{bmatrix} \quad (25)$$

Analogous to the restriction on the Poisson's ratio in the isotropic case, the energy parameters $\epsilon_i^{n,t} \geq 0$ in the transverse isotropic case need to satisfy $C_{66} = (C_{11} - C_{12})/2$, which entails, for the lattices studied here

Table 2. Energy Parameters Calibration

Energy parameters	Three-dimensional		Two-dimensional	
	$-1 \leq \nu \leq 0$	$0 \leq \nu \leq 1/4$	$-2/3 \leq \nu \leq 0$	$0 \leq \nu \leq 1/3$
e_1^n	$\frac{(n-1)^2 Ea_0^3}{n^2(1-2\nu)}$	$\frac{(n-1)^2(1-3\nu)Ea_0^3}{n^2(1+\nu)(1-2\nu)}$	$\frac{[n(2+3\nu)-2(1+\nu)]Ea_0^3}{4n(1-\nu^2)}$	$\frac{[n(2-3\nu)-2(1-\nu)]Ea_0^3}{4n(1-\nu^2)}$
e_4^n	0	$\frac{2(n-1)\nu Ea_0^3}{n(1+\nu)(1-2\nu)}$	0	$\frac{\nu Ea_0^3}{1-\nu^2}$
e_{10}^n	0	0	0	0
e_1^t	$\frac{(n-1)^2 Ea_0^3}{n^2(1+\nu)(1-2\nu)}$	$\frac{(n-1)^2(1-4\nu)Ea_0^3}{n^2(1+\nu)(1-2\nu)}$	$\frac{(n-1+\nu)Ea_0^3}{2n(1-\nu^2)}$	$\frac{(n-1)(1-3\nu)Ea_0^3}{2n(1-\nu^2)}$
e_4^t	$-\frac{2(n-1)\nu Ea_0^3}{n(1+\nu)(1-2\nu)}$	0	$\frac{-\nu Ea_0^3}{1-\nu^2}$	0
e_{10}^t	0	0	0	0

**Fig. 2.** (a) Finite size effect; (b and c) 3D and 2D dimensionless stiffness constants (C_{ij}/E) as a function of the Poisson's ratio ($n = 21$); theoretical values (solid lines), numerical values (symbols)

$$\begin{aligned} C_{12} &\leq C_{66} \\ C_{13} &\leq C_{44} \end{aligned} \quad (26)$$

Validation

To validate the derived calibration procedure, the analytical expressions thus derived are compared with numerical simulations. Details about the numerical implementation are given in Appendix II. Simulations are carried out on simulation boxes of varying size n using a D3Q18 3D lattice. These simulation boxes are subject to deformations in six directions in order to obtain the different stiffness constants C_{ij} .

Specifically, Fig. 2(a) shows the dimensionless Young's modulus values Ea_0^3/ϵ_1^n obtained analytically and numerically as a function of size n of the D3Q18 3D lattice. In this simulation, the Poisson's ratio was chosen equal to $1/4$, corresponding to the central-force lattice model ($e_1^t = 0$). The figure shows that the elastic modulus tends asymptotically toward a constant value in the continuum limit, and is in perfect agreement with the analytical

functional form derived previously for the isotropic case. In contrast with the numerical simulations, the analytical expression permits a direct evaluation of the elastic modulus in the continuum limit from the value at a given discretization level (size n).

Moreover, Figs. 2(b and c) compare the stiffness constants measured with LEM (using the energy parameters given in Table 2) to the analytical values. The figures display a perfect agreement for a wide range of Poisson's ratio, and validate the proposed potential calibration procedure for the energy parameters $e_i^{n,t}$ within the limit defined by Eq. (22).

Application: Stress Field around a Crack

For purposes of application, the proposed LEM approach is applied to a classical problem of continuum elasticity, the stress field around a crack, viewed as a geometric discontinuity. The rationale of this sample application is that LEM removes by its very discrete nature the geometric discontinuity and the associated stress singularity that defines at the crack tip the well-known near-tip singular stress solution. The investigation thus departs from the following

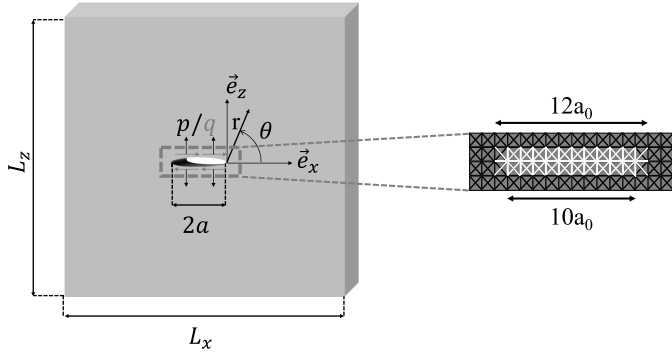


Fig. 3. Griffith crack (length $2a$) subjected to a pressure p and a shear q and Griffith crack in LEM ($n_a = 5$); white links are links with zero stiffness ($e^{n,t} = 0$)

point of inquiry: is LEM able to capture this asymptotic stress and crack opening behavior without considering the geometric discontinuity? A positive answer to this question would open the way to using LEM, e.g., for the determination of stress intensity factors (SIFs), which are used in linear-elastic fracture mechanics (LEFM) for evaluating the risk of fracture.

For purposes of analysis, the problem of a quasi-2D (plane stress) slit crack (or Griffith crack) of length $2a/L \ll 1$ is considered where L is the dimension of the solid (Fig. 3) of Young's modulus E and Poisson's ratio ν . The crack is subjected on its upper (+) and lower (-) lip to a pressure p and/or a shear stress q ; i.e., $\boldsymbol{\sigma} \cdot \mathbf{n} = \pm p\mathbf{e}_y \pm q\mathbf{e}_x$ with \mathbf{n} being the unit normal to the crack surface. For the continuum case, the near-tip linear-elastic isotropic stress fields for a crack in the plane $z = 0$ and oriented in the x -direction are well known (e.g., Sun and Jin 2012)

$$\begin{aligned}\sigma_{xx} &= \frac{K_I}{\sqrt{2\pi r}} \cos \frac{\vartheta}{2} \left(1 - \sin \frac{3\vartheta}{2} \sin \frac{\vartheta}{2} \right) - \frac{K_{II}}{\sqrt{2\pi r}} \sin \frac{\vartheta}{2} \left(2 + \cos \frac{3\vartheta}{2} \cos \frac{\vartheta}{2} \right) \\ \sigma_{zz} &= \frac{K_I}{\sqrt{2\pi r}} \cos \frac{\vartheta}{2} \left(1 + \sin \frac{3\vartheta}{2} \sin \frac{\vartheta}{2} \right) + \frac{K_{II}}{\sqrt{2\pi r}} \sin \frac{\vartheta}{2} \cos \frac{3\vartheta}{2} \cos \frac{\vartheta}{2} \\ \sigma_{xz} &= \frac{K_I}{\sqrt{2\pi r}} \cos \frac{\vartheta}{2} \cos \frac{3\vartheta}{2} \sin \frac{\vartheta}{2} + \frac{K_{II}}{\sqrt{2\pi r}} \cos \frac{\vartheta}{2} \left(1 - \sin \frac{3\vartheta}{2} \sin \frac{\vartheta}{2} \right)\end{aligned}\quad (27)$$

as well as the displacements

$$\begin{aligned}\xi_x &= \frac{K_I}{8G\pi} \sqrt{2\pi r} \left[(2\kappa - 1) \cos \frac{\vartheta}{2} - \cos \frac{3\vartheta}{2} \right] \\ &\quad + \frac{K_{II}}{8G\pi} \sqrt{2\pi r} \left[(2\kappa + 3) \sin \frac{\vartheta}{2} + \sin \frac{3\vartheta}{2} \right] \\ \xi_z &= \frac{K_I}{8G\pi} \sqrt{2\pi r} \left[(2\kappa + 1) \sin \frac{\vartheta}{2} - \sin \frac{3\vartheta}{2} \right] \\ &\quad - \frac{K_{II}}{8G\pi} \sqrt{2\pi r} \left[(2\kappa - 3) \cos \frac{\vartheta}{2} + \cos \frac{3\vartheta}{2} \right]\end{aligned}\quad (28)$$

where $\kappa =$ dimensionless coefficient equal to $3 - 4\nu$ in plane strain and to $(3 - \nu)/(1 + \nu)$ in plane stress. The origin of the coordinate system (r, ϑ) is at the crack tip; and K_I and K_{II} are the Mode I and Mode II SIFs. They are defined asymptotically either from the stresses

$$K_{I,II} = \lim_{r \rightarrow 0} \sqrt{2\pi r} \sigma_{zz,xz}(r, \vartheta = 0) \quad (29)$$

or from the displacement jumps along the crack lips, $[[\xi_{x,z}]](r) = \xi_{x,z}(r, \vartheta = \pi) - \xi_{x,z}(r, \vartheta = -\pi)$

$$K_{I,II} = \lim_{r \rightarrow 0} \frac{G}{1 + \kappa} \sqrt{\frac{2\pi}{r}} [[\xi_{z,x}]](r) \quad (30)$$

Given the 2D geometry of the problem, simulations were performed with a quasi-2D lattice of size $L_x = L_z = L = 400a_0$ ($n = 401$ nodes per side) containing a crack of half-length $a = n_a a_0$, $n_a \in \mathbb{N}$, with $n_a \ll 400$. All mass points on the crack surfaces ($x \in [-a, a], z = 0$) have zero energy parameters ($e_i^{n,t} = 0$). A pressure is imposed on the nodes directly above and below the crack plane. As can be seen in Fig. 3, the actual crack half-length is ill defined due to the discrete nature of LEM removing a clear geometric discontinuity. The effective crack half-length a_{eff} is somewhere in between $n_a a_0$ and $(n_a + 1)a_0$. With the geometric discontinuity removed, it is readily understood that the near-tip solution in Eq. (27) will fail to represent the stress field obtained by the discrete lattice model. Instead, the stress fields thus obtained from the simulations need to be compared with Muskhelishvili's exact solution of the Griffith crack problem derived using Plemelj formula and Cauchy integrals (Muskhelishvili 1953), or with England and Green's solution obtained by using simple integral equations and real variable integration (England and Green 1963). The comparison of the LEM results with Muskhelishvili's exact solution is shown in Fig. 4 for a pure Mode I loading. In the simulations, $n_a = 5$ was considered, whereas the comparison is shown by evaluating the analytical solution for an effective crack half-length $a_{\text{eff}} = a_0(n_a + 0.7)$, which provided a perfect match between numerical and analytical hoop stress $\sigma_{\vartheta\vartheta} = \sigma_{zz}$ in the crack

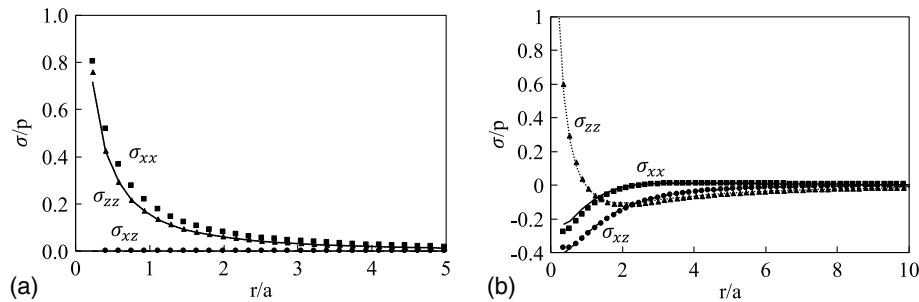


Fig. 4. (a) Stresses in the crack plane ($\theta = 0$) in Mode I; (b) normal to the crack plane ($\theta = \pi/2$) in Mode I; exact solution (lines) and numerical results from LEM (symbols)

Table 3. Error on the Stress Intensity Factors

ν	n_a	p/E	$r_0^\sigma/a_{\text{eff}}$	$(K_I - K_I^\sigma)/K_I$ (%)	r_0^ξ/a_{eff}	$(K_I - K_I^\xi)/K_I$ (%)
1/3	5	2×10^{-4}	0.30	41.4	0.12	4.8
1/4	5	2×10^{-4}	0.30	39.0	0.12	7.2
1/3	6	2×10^{-4}	0.25	38.0	0.10	4.1
1/4	6	2×10^{-4}	0.25	35.6	0.10	6.2
1/3	7	2×10^{-4}	0.22	35.0	0.09	3.5
1/4	7	2×10^{-4}	0.22	32.7	0.09	5.4
1/3	8	2×10^{-4}	0.20	32.5	0.08	3.0
1/4	8	2×10^{-4}	0.20	30.2	0.08	4.8
1/3	9	2×10^{-4}	0.18	30.4	0.07	2.6
1/4	9	2×10^{-4}	0.18	28.0	0.07	4.3
1/3	10	2×10^{-4}	0.16	28.4	0.07	2.3
1/4	10	2×10^{-4}	0.16	26.1	0.07	3.8
1/3	10	1×10^{-4}	0.16	28.4	0.07	2.3
1/3	10	4×10^{-4}	0.16	28.4	0.07	2.3

plane. This agreement not only holds for stresses in the crack plane ($\vartheta = 0$), but also for stresses perpendicular to the crack plane ($\vartheta = \pi/2$). This means that the LEM approach is able to accurately capture the exact solution. A similar agreement was found for a pure Mode II loading ($p = 0$, $q \neq 0$).

Because the exact solution degenerates asymptotically to the singular near-tip solution, it is tempting to check whether the LEM approach provides a means to determine the stress intensity factors, K_I and K_{II} , from either stress definition in Eq. (29)

$$\begin{aligned} K_I^\sigma &\approx \sigma_{zz}(x = a_{\text{eff}} + r_0^\sigma, z = 0) \sqrt{2\pi r_0^\sigma} \\ K_{II}^\sigma &\approx \sigma_{xz}(x = a_{\text{eff}} + r_0^\sigma, z = 0) \sqrt{2\pi r_0^\sigma} \end{aligned} \quad (31)$$

or from their displacement definition in Eq. (30), considering the displacement jump along the crack surface

$$\begin{aligned} K_I^\xi &\approx \frac{E}{4} \sqrt{\frac{\pi}{2r_0^\xi}} [\xi_z(x = a_{\text{eff}} - r_0^\xi, z = a_0) - \xi_z(x = a_{\text{eff}} - r_0^\xi, z = -a_0)] \\ K_{II}^\xi &\approx \frac{E}{4} \sqrt{\frac{\pi}{2r_0^\xi}} [\xi_x(x = a_{\text{eff}} - r_0^\xi, z = a_0) - \xi_x(x = a_{\text{eff}} - r_0^\xi, z = -a_0)] \end{aligned} \quad (32)$$

with $r_0^{\sigma,\xi}/a \ll 1$. In LEM, the first node where a meaningful stress measure can be obtained is located at $r_0^\sigma = (n_a + 2)a_0 - a_{\text{eff}}$, and the first node where a meaningful crack opening measure can be obtained is at $r_0^\xi = a_{\text{eff}} - n_a a_0$. For a good assessment of the SIFs, the condition $r_0^{\sigma,\xi}/a \ll 1$ would thus require a very fine discretization ($a_0/a \ll 1$ keeping $2a/L \ll 1$). This is particularly true for a SIF determination using the stress measure (K_I^σ): the error made on the exact stress $\sigma_{zz}(r, \vartheta = 0)$ using the asymptotic development in Eq. (27) is indeed $\sim 5\%$ at a distance to the crack tip on the order of $r = a/1,000$ and as large as $\sim 95\%$ at a distance $r = a/5$. In contrast, the use of the crack opening for the determination of the SIFs (K_I^ξ) is more accurate. The error made on the exact crack opening $[[\xi_z]](r)$ using the displacement asymptotic development in Eq. (28) is indeed only $\sim 5\%$ at a distance to the crack tip of $r = a/5$. The results of the determination of the SIFs ($K_I^{\sigma,\xi}$) of Griffith cracks using the results from LEM in Eqs. (31) and (32) are compared with the analytical value ($K_I = p\sqrt{\pi a}$) in Table 3 for cracks of different lengths ($n_a = 5, 6, 7, 8, 9, 10$), different pressures ($p/E = 1 \times 10^{-4}, 2 \times 10^{-4}, 4 \times 10^{-4}$) and different Poisson's ratios ($\nu = 1/3, 1/4$). As expected, it is found that K_I^ξ gives a much better estimate of the SIF than K_I^σ . That is, despite the removal of the stress singularities (due to the discrete nature

of the method) associated with the geometric discontinuity, the LEM approach provides good estimates of SIFs using the displacement jump definition [Eq. (32)], provided a discretization with $a_0/a < 0.1$.

Conclusion

Thus far, the LEM emerges as a powerful means to track the mechanical interactions between material points in a discrete way. While classical approaches defined those interactions from beam-type analogies, the method has clearly more to offer when set in the context of effective potentials, of which the harmonic case is but a Taylor expansion around the (undeformed) equilibrium state. This framework provides a means to set the method onto a path toward modeling the actual physics interactions between phases, within the limits defined by the geometric discretization of regular or irregular lattices that entail certain limits on accessible effective mechanics properties, such as the restrictions on Poisson's ratios for isotropic materials ($-2/3 \leq \nu \leq 1/3$ in 2D and $-1 < \nu \leq 1/4$ in 3D), or on the elasticity of transverse isotropic materials (achieved with both D3Q26 and D3Q18 lattices). The following was thus shown:

- **Potential calibration:** The proposed improvements contribute to the development of a rational framework linking potential parameters that define the local interactions (the two- and three-body energy parameters, ϵ^n and ϵ^l) to effective material properties of an assembly of links.
- **Elasticity:** LEM converges to the homogeneous continuum elasticity model as the level of discretization of matter into mass points tends toward infinity. This means that LEM can be used, at a given discretization level of matter, to correct for finite size effects without compromising the accuracy of the elasticity solution.
- **Linear-elastic fracture mechanics:** The accuracy of LEM is such that it is able to capture continuum-scale quantities, such as SIFs, even if its very discrete nature removes geometric discontinuities that provoke stress singularities. In fact, the displacement solution derived from LEM is perfectly apt to quantitatively assess SIFs from a coarse discretization that does not respect the classical assumptions of scale separability of continuum mechanics.
- **Nonharmonic interaction:** While LEM has been classically employed with harmonic potentials to capture stretch and bending modes, the reformulation of LEM in the framework of effective potentials clearly shows that the classical LEM is but a Taylor expansion of said interactions around the undeformed configurations. Otherwise said, the framework suggests that LEM can be used—in a bottom-up fashion—to integrate smaller-scale interactions by means of coarse graining (e.g., Masoero et al. 2012; Ioannidou et al. 2016) into mesoscale simulations on the lattice.

While the theoretical developments presented here were only concerned with homogeneous materials, these advances are expected to be invaluable in the application of the method to heterogeneous materials, in which the method thus enhanced provides a means to assess the impact of different phases and disorders on effective properties, far beyond the classical continuum assumptions. Specifically, with its strengths and limitations thus defined, the proposed LEM is well suited for the study of multiphase materials whose microtextural information is obtained by, e.g., X-ray micro-computed tomography, at a scale where the assumption of scale separation required by continuum-based models is violated. This is the focus of forthcoming developments.

Appendix I. Transformation from Global to Local System of Coordinates

The transformation between the local system of coordinates of link $0i$, $(\mathbf{e}_n^i, \mathbf{e}_b^i, \mathbf{e}_t^i)$ and the global system of coordinates $(\mathbf{e}_x, \mathbf{e}_y, \mathbf{e}_z)$ is done by the following equations:

$$\mathbf{e}_n^i = \mathbf{P}_{1i}^n \mathbf{e}_x + \mathbf{P}_{2i}^n \mathbf{e}_y + \mathbf{P}_{3i}^n \mathbf{e}_z \quad \mathbf{e}_b^i = \mathbf{P}_{1i}^b \mathbf{e}_x + \mathbf{P}_{2i}^b \mathbf{e}_y + \mathbf{P}_{3i}^b \mathbf{e}_z \quad \mathbf{e}_t^i = \mathbf{P}'_{1i} \mathbf{e}_x + \mathbf{P}'_{2i} \mathbf{e}_y + \mathbf{P}'_{3i} \mathbf{e}_z \quad (33)$$

where the matrices $\mathbf{P}^{n,b,t}$ are given by

$$\mathbf{P}^n = \begin{bmatrix} 1 & 0 & 0 & \frac{\sqrt{2}}{2} & -\frac{\sqrt{2}}{2} & 0 & 0 & \frac{\sqrt{2}}{2} & \frac{\sqrt{2}}{2} & \frac{\sqrt{3}}{3} & \frac{\sqrt{3}}{3} & -\frac{\sqrt{3}}{3} & -\frac{\sqrt{3}}{3} \\ 0 & 1 & 0 & \frac{\sqrt{2}}{2} & \frac{\sqrt{2}}{2} & \frac{\sqrt{2}}{2} & \frac{\sqrt{2}}{2} & 0 & 0 & \frac{\sqrt{3}}{3} & \frac{\sqrt{3}}{3} & \frac{\sqrt{3}}{3} & \frac{\sqrt{3}}{3} \\ 0 & 0 & 1 & 0 & 0 & \frac{\sqrt{2}}{2} & -\frac{\sqrt{2}}{2} & \frac{\sqrt{2}}{2} & -\frac{\sqrt{2}}{2} & \frac{\sqrt{3}}{3} & -\frac{\sqrt{3}}{3} & -\frac{\sqrt{3}}{3} & \frac{\sqrt{3}}{3} \end{bmatrix} \quad (34)$$

$$\mathbf{P}^b = \begin{bmatrix} 1 & 0 & 0 & \frac{\sqrt{2}}{2} & -\frac{\sqrt{2}}{2} & 0 & 0 & \frac{\sqrt{2}}{2} & \frac{\sqrt{2}}{2} & \frac{\sqrt{3}}{3} & \frac{\sqrt{3}}{3} & -\frac{\sqrt{3}}{3} & -\frac{\sqrt{3}}{3} \\ 0 & 1 & 0 & \frac{\sqrt{2}}{2} & \frac{\sqrt{2}}{2} & \frac{\sqrt{2}}{2} & \frac{\sqrt{2}}{2} & 0 & 0 & \frac{\sqrt{3}}{3} & \frac{\sqrt{3}}{3} & \frac{\sqrt{3}}{3} & \frac{\sqrt{3}}{3} \\ 0 & 0 & 1 & 0 & 0 & \frac{\sqrt{2}}{2} & -\frac{\sqrt{2}}{2} & \frac{\sqrt{2}}{2} & -\frac{\sqrt{2}}{2} & \frac{\sqrt{3}}{3} & -\frac{\sqrt{3}}{3} & -\frac{\sqrt{3}}{3} & \frac{\sqrt{3}}{3} \end{bmatrix} \quad (35)$$

$$\mathbf{P}' = \begin{bmatrix} 0 & 0 & 0 & 0 & 0 & 1 & 1 & 0 & 0 & \frac{\sqrt{6}}{6} & -\frac{\sqrt{6}}{6} & \frac{\sqrt{6}}{6} & -\frac{\sqrt{6}}{6} \\ 0 & 0 & 1 & 0 & 0 & 0 & 0 & 1 & 1 & \frac{\sqrt{6}}{6} & -\frac{\sqrt{6}}{6} & -\frac{\sqrt{6}}{6} & \frac{\sqrt{6}}{6} \\ 1 & 1 & 0 & 1 & 1 & 0 & 0 & 0 & 0 & -\frac{\sqrt{6}}{3} & -\frac{\sqrt{6}}{3} & -\frac{\sqrt{6}}{3} & -\frac{\sqrt{6}}{3} \end{bmatrix} \quad (36)$$

The nodal displacements of a lattice under uniform deformations are obtained through the following matrices:

$$\mathbf{\Delta}^n = \begin{bmatrix} 1 & 0 & 0 & \frac{\sqrt{2}}{2} & \frac{\sqrt{2}}{2} & 0 & 0 & \frac{\sqrt{2}}{2} & \frac{\sqrt{2}}{2} & \frac{\sqrt{3}}{3} & \frac{\sqrt{3}}{3} & \frac{\sqrt{3}}{3} & \frac{\sqrt{3}}{3} \\ 0 & 1 & 0 & \frac{\sqrt{2}}{2} & \frac{\sqrt{2}}{2} & \frac{\sqrt{2}}{2} & \frac{\sqrt{2}}{2} & 0 & 0 & \frac{\sqrt{3}}{3} & \frac{\sqrt{3}}{3} & \frac{\sqrt{3}}{3} & \frac{\sqrt{3}}{3} \\ 0 & 0 & 1 & 0 & 0 & \frac{\sqrt{2}}{2} & \frac{\sqrt{2}}{2} & \frac{\sqrt{2}}{2} & \frac{\sqrt{2}}{2} & \frac{\sqrt{3}}{3} & \frac{\sqrt{3}}{3} & \frac{\sqrt{3}}{3} & \frac{\sqrt{3}}{3} \\ 0 & 0 & 0 & \frac{\sqrt{2}}{2} & -\frac{\sqrt{2}}{2} & 0 & 0 & 0 & 0 & \frac{\sqrt{3}}{3} & \frac{\sqrt{3}}{3} & -\frac{\sqrt{3}}{3} & -\frac{\sqrt{3}}{3} \\ 0 & 0 & 0 & 0 & 0 & 0 & 0 & \frac{\sqrt{2}}{2} & -\frac{\sqrt{2}}{2} & \frac{\sqrt{3}}{3} & -\frac{\sqrt{3}}{3} & \frac{\sqrt{3}}{3} & -\frac{\sqrt{3}}{3} \\ 0 & 0 & 0 & 0 & 0 & \frac{\sqrt{2}}{2} & -\frac{\sqrt{2}}{2} & 0 & 0 & \frac{\sqrt{3}}{3} & -\frac{\sqrt{3}}{3} & -\frac{\sqrt{3}}{3} & \frac{\sqrt{3}}{3} \end{bmatrix} \quad (37)$$

$$\Delta^b = \begin{bmatrix} 0 & 0 & 0 & -\frac{\sqrt{2}}{2} & \frac{\sqrt{2}}{2} & 0 & 0 & \frac{\sqrt{2}}{2} & -\frac{\sqrt{2}}{2} & \frac{\sqrt{2}}{2} & \frac{\sqrt{2}}{2} & -\frac{\sqrt{2}}{2} & -\frac{\sqrt{2}}{2} \\ 0 & 0 & 0 & \frac{\sqrt{2}}{2} & -\frac{\sqrt{2}}{2} & -\frac{\sqrt{2}}{2} & \frac{\sqrt{2}}{2} & 0 & 0 & -\frac{\sqrt{2}}{2} & -\frac{\sqrt{2}}{2} & \frac{\sqrt{2}}{2} & \frac{\sqrt{2}}{2} \\ 0 & 0 & 0 & 0 & 0 & \frac{\sqrt{2}}{2} & -\frac{\sqrt{2}}{2} & -\frac{\sqrt{2}}{2} & \frac{\sqrt{2}}{2} & 0 & 0 & 0 & 0 \\ 0 & -1 & 0 & -\frac{\sqrt{2}}{2} & -\frac{\sqrt{2}}{2} & 0 & 0 & 0 & 0 & \frac{\sqrt{2}}{2} & \frac{\sqrt{2}}{2} & \frac{\sqrt{2}}{2} & \frac{\sqrt{2}}{2} \\ 0 & 0 & 1 & 0 & 0 & 0 & 0 & \frac{\sqrt{2}}{2} & \frac{\sqrt{2}}{2} & \frac{\sqrt{2}}{2} & -\frac{\sqrt{2}}{2} & -\frac{\sqrt{2}}{2} & \frac{\sqrt{2}}{2} \\ 0 & 0 & 0 & 0 & 0 & -\frac{\sqrt{2}}{2} & -\frac{\sqrt{2}}{2} & 0 & 0 & -\frac{\sqrt{2}}{2} & \frac{\sqrt{2}}{2} & -\frac{\sqrt{2}}{2} & \frac{\sqrt{2}}{2} \end{bmatrix} \quad (38)$$

$$\Delta^t = \begin{bmatrix} 0 & 0 & 0 & 0 & 0 & 0 & 0 & 0 & 0 & 0 & \frac{\sqrt{6}}{6} & -\frac{\sqrt{6}}{6} & -\frac{\sqrt{6}}{6} & \frac{\sqrt{6}}{6} \\ 0 & 0 & 0 & 0 & 0 & 0 & 0 & 0 & 0 & 0 & \frac{\sqrt{6}}{6} & -\frac{\sqrt{6}}{6} & -\frac{\sqrt{6}}{6} & \frac{\sqrt{6}}{6} \\ 0 & 0 & 0 & 0 & 0 & 0 & 0 & 0 & 0 & -\frac{\sqrt{6}}{3} & \frac{\sqrt{6}}{3} & \frac{\sqrt{6}}{3} & -\frac{\sqrt{6}}{3} \\ 0 & 0 & 0 & 0 & 0 & 1 & 1 & 0 & 0 & \frac{\sqrt{6}}{6} & -\frac{\sqrt{6}}{6} & \frac{\sqrt{6}}{6} & -\frac{\sqrt{6}}{6} \\ 0 & 0 & 0 & 0 & 0 & 1 & -1 & 0 & 0 & \frac{\sqrt{6}}{6} & \frac{\sqrt{6}}{6} & -\frac{\sqrt{6}}{6} & -\frac{\sqrt{6}}{6} \\ 0 & 0 & 1 & 0 & 0 & 0 & 0 & 1 & -1 & \frac{\sqrt{6}}{6} & \frac{\sqrt{6}}{6} & \frac{\sqrt{6}}{6} & \frac{\sqrt{6}}{6} \end{bmatrix} \quad (39)$$

Appendix II. Numerical Implementation

Details about the numerical implementation of the LEM method for harmonic potentials are provided herein.

To study the elastic response of a solid under an external load (prescribed traction on the boundary $\partial\Omega_{T^d}$ and/or prescribed displacements on the boundary $\partial\Omega_{\xi^d}$), the theorem of minimum potential energy is employed

$$E_{\text{pot}}^{\text{sol}}(\epsilon, \xi) = \min_{\xi' \in \text{K.A.}} E_{\text{pot}}(\epsilon', \xi) \quad (40)$$

where K.A. = set of kinematically admissible displacement fields that satisfy displacement boundary conditions

$$\text{K.A.} = \{\xi \text{ continuous such that } \xi = \xi^d \text{ on } \partial\Omega_{\xi^d}\} \quad (41)$$

whereas ϵ = strain; and ϵ_{pot} = potential energy

$$E_{\text{pot}}(\epsilon', \xi') = U(\epsilon') - W(\xi') \quad (42)$$

with $U(\epsilon')$ = free energy; and $W(\xi')$ = external work by body forces \mathbf{b} and prescribed traction \mathbf{T}^d ; that is, $W(\xi') = \int_{\Omega} \xi' \cdot \mathbf{b} d\Omega + \int_{\partial\Omega_{T^d}} \xi' \cdot \mathbf{T}^d da$. In the case when only displacements are prescribed on the boundaries, only the free energy term U contributes to the potential energy.

In the numerical implementation, for a structure of size $L_x L_y L_z$, the volume is discretized for a given grid size $a_0 = L_x / (n_x - 1)$. The $N = n_x n_y n_z$ nodes i of coordinates $\{\tilde{r}_i\} = (\tilde{x}, \tilde{y}, \tilde{z})$ are defined in the reference configuration, with

$(\tilde{x}, \tilde{y}, \tilde{z}) \in \{0, 1, \dots, n_{x,y,z} - 1\}$. The notation $\tilde{\cdot}$ stands for the quantities in *code units* for energies $U = \tilde{U} a_0^3$, forces $f = \tilde{f} a_0^2$, lengths $l = \tilde{l} a_0$, and stresses $\sigma = \tilde{\sigma}$. A one-to-one relation between node index i and its coordinates: $i = \tilde{x} + n_x \tilde{y} + n_x n_y \tilde{z}$ is defined. Each node has six degrees of freedom: three displacements $\tilde{\delta}_i^\alpha$ and three rotations $\tilde{\theta}_i^\alpha$, $\alpha \in \{x, y, z\}$, that are stored in a $6N$ vector $\{\tilde{d}\}$ such that $\tilde{d}_{6i} = \tilde{\delta}_i^x$, $\tilde{d}_{6i+1} = \tilde{\delta}_i^y$, $\tilde{d}_{6i+2} = \tilde{\delta}_i^z$, $\tilde{d}_{6i+3} = \tilde{\theta}_i^x$, $\tilde{d}_{6i+4} = \tilde{\theta}_i^y$, and $\tilde{d}_{6i+5} = \tilde{\theta}_i^z$. Node i has N_i^b neighbors j , with which it interacts via link ij of energy parameters $\tilde{c}_{ij}^{n;t} = \tilde{c}_{ji}^{n;t}$ (that depend on the phase attributed to nodes i and j) and of orientation $\{\tilde{r}_{ij}\} = \{\tilde{r}_j\} - \{\tilde{r}_i\}$. The forces and moments at node i are obtained by summing the contribution of all links

$$\tilde{\mathbf{F}}_i = \sum_{j=1}^{N_i^b} \tilde{\mathbf{F}}_i^j \quad \tilde{\mathbf{M}}_i = \sum_{j=1}^{N_i^b} \tilde{\mathbf{M}}_i^j \quad (43)$$

where $\tilde{\mathbf{F}}_i^j$ and $\tilde{\mathbf{M}}_i^j$ are given by Eqs. (5) and (6). These are also stored in a $6N$ vector, $\{\tilde{f}\}$, such that $\tilde{f}_{6i} = \tilde{F}_i^x$, $\tilde{f}_{6i+1} = \tilde{F}_i^y$, $\tilde{f}_{6i+2} = \tilde{F}_i^z$, $\tilde{f}_{6i+3} = \tilde{M}_i^x$, $\tilde{f}_{6i+4} = \tilde{M}_i^y$, and $\tilde{f}_{6i+5} = \tilde{M}_i^z$.

In addition, the nodes where boundary conditions (forces or displacements) are imposed are defined by considering the sets $\mathcal{N}_{\tilde{f}^d} = \{(j, \tilde{f}^d) | \tilde{f}_j = \tilde{f}^d\}$ (nodes where a force is imposed) and $\mathcal{N}_{\tilde{\delta}^d} = \{(j, \tilde{\delta}^d) | \tilde{d}_j = \tilde{\delta}^d\}$ (nodes where a displacement is imposed), with $j \in \{0, \dots, 6N - 1\}$.

The potential energy is written in LEM as

$$E_{\text{pot}} = \frac{1}{2} \sum_{i=1}^N \sum_{j=1}^{N_j^b} \tilde{U}_{ij}(\tilde{\mathbf{d}}) - \sum_{(i, \tilde{f}^d) \in \mathcal{N}_{\tilde{f}^d}} \tilde{d}_i \tilde{f}^d \quad (44)$$

where the factor 1/2 prevents counting the contribution of each link twice. The first term in Eq. (44) is the free energy, while the second one is the work done by external forces.

The numerical implementation of the theorem of potential energy consists of finding the vector $\{\tilde{\mathbf{d}}\}$ that minimizes \tilde{E}_{pot} under the constraint $\tilde{d}_j = \tilde{\delta}^d$ for $(j, \tilde{\delta}^d) \in \mathcal{N}_{\tilde{\delta}^d}$. This energy minimization is performed numerically, using a nonlinear conjugate gradient method, the Fletcher-Reeves-Polak-Ribiere method. It can also be achieved using molecular simulation codes. Once the solution $\{\tilde{\mathbf{d}}\}$ to the problem is found, the stress tensor at each node $\tilde{\boldsymbol{\sigma}}_i$ and the total stress $\tilde{\boldsymbol{\sigma}}$ are obtained using the virial definition

$$\tilde{\boldsymbol{\sigma}}_i = \sum_{j=1}^{N_j^b} \tilde{\mathbf{r}}_{ij} \otimes \tilde{\mathbf{F}}_i^j; \quad \tilde{\boldsymbol{\sigma}} = \frac{1}{2(n_x - 1)(n_y - 1)(n_z - 1)} \sum_{i=1}^N \tilde{\boldsymbol{\sigma}}_i \quad (45)$$

Acknowledgments

Research carried out within the X-Shale Hub at MIT, the Science and Engineering of Gas Shale, a collaboration between Shell, Schlumberger, and MIT, enabled through MIT's Energy Initiative. Farhang Radjaï would like to acknowledge the support of the ICoME2 Labex (ANR-11-LABX-0053) and the A*MIDEX projects (ANR-11-IDEX-0001-02) cofunded by the French program Investissements d'Avenir, managed by the French National Research Agency (ANR). The authors would like to acknowledge Vincent Richefeu (Université Joseph Fourier), Jean-Yves Delenne (Montpellier SupAgro), and Saeid Nezamabadi (Université de Montpellier), who provided the backbone of the LEM code used for the simulations.

References

- Affes, R., Delenne, J.-Y., Monerie, Y., Radja, F., and Topin, V. (2012). "Tensile strength and fracture of cemented granular aggregates." *Eur. Phys. J. E*, 35(11), 117.
- Avendaño, C., Lafitte, T., Galindo, A., Adjiman, C. S., Jackson, G., and Müller, E. A. (2011). "SAFT- γ force field for the simulation of molecular fluids. 1: A single-site coarse grained model of carbon dioxide." *J. Phys. Chem. B*, 115(38), 11154–11169.
- Bolander, J. E., Jr., and Saito, S. (1998). "Fracture analyses using spring networks with random geometry." *Eng. Fract. Mech.*, 61(5), 569–591.
- Christoffersen, J., Mehrabadi, M. M., and Nemat-Nasser, S. (1981). "A micromechanical description of granular material behavior." *J. Appl. Mech.*, 48(2), 339–344.

- Desrués, J., Viggiani, G., and Besuelle, P. (2006). *Advances in X-ray tomography for geomaterials*, ISTE, London.
- D'Humières, D., Ginzburg, I., Krafczyk, M., Lallemand, P., and Luo, L. S. (2002). "Multiple-relaxation-time lattice Boltzmann models in three dimensions." *Philos. Trans. R. Soc. London, Ser. A*, 360(1792), 437–451.
- England, A. H., and Green, A. E. (1963). "Some two dimensional punch and crack problems in classical elasticity." *Math. Proc. Cambridge Philos. Soc.*, 59(2), 489–500.
- Falk, K., Pellenq, R., Ulm, F.-J., and Coasne, B. (2015). "Effect of chain length and pore accessibility on alkane adsorption in kerogen." *Energy Fuels*, 29(12), 7889–7896.
- Greaves, G. N., Greer, A. L., Lakes, R. S., and Rouxel, T. (2011). "Poisson's ratio and modern materials." *Nat. Mater.*, 10(11), 823–837.
- Hansen, A., Roux, S., and Herrmann, H. J. (1989). "Rupture of central-force lattices." *J. Phys.*, 50(7), 733–744.
- Hrennikoff, A. (1941). "Solution of problems of elasticity by the framework method." *J. Appl. Mech.*, 8(4), 169–175.
- Ioannidou, K., et al. (2016). "Mesoscale texture of cement hydrates." *Proc. Natl. Acad. Sci.*, 113(8), 2029–2034.
- Kosteski, L., Barrios D'Ambra, R., and Iturrioz, I. (2012). "Crack propagation in elastic solids using the truss-like discrete element method." *Int. J. Fract.*, 174(2), 139–161.
- Lilliu, G., and van Mier, J. G. M. (2003). "3D lattice type fracture model for concrete." *Eng. Fract. Mech.*, 70(7), 927–941.
- Lilliu, G., van Mier, J. G. M., and van Vliet, M. R. A. (1999). "Numerical characterization of the elastic properties of heterogeneous materials with a 3D lattice model." *Trans. Modell. Simul.*, 21, 515–524.
- Masoero, E., Del Gado, E., Pellenq, R., Ulm, F.-J., and Yip, S. (2012). "Nanostructure and nanomechanics of cement: Polydisperse colloidal packing." *Phys. Rev. Lett.*, 109(15), 3–6.
- Monfared, S., Laubie, H., Radjaï, F., Pellenq, R., and Ulm, F.-J. (2016). "Mesoscale poroelasticity of heterogeneous media." *J. Nanomech. Micromech.*, in press.
- Muskhelishvili, N. I. (1953). *Some basic problems of mathematical theory of elasticity*, Noordhoff, Groningen, Netherlands.
- Nayfeh, A. H., and Hefzy, M. S. (1978). "Continuum modeling of three-dimensional truss-like space structures." *AIAA J.*, 16(8), 779–787.
- Schlangen, E., and Garboczi, E. J. (1996). "New method for simulating fracture using an elastically uniform random geometry lattice." *Int. J. Eng. Sci.*, 34(10), 1131–1144.
- Schlangen, E., and Garboczi, E. J. (1997). "Fracture simulations of concrete using lattice models: Computational aspects." *Eng. Fract. Mech.*, 57(2), 319–332.
- Sun, C.-T., and Jin, Z. (2012). *Fracture mechanics*, Academic, Waltham, MA.
- Thomas, J. F., Jr. (1971). "Failure of the Cauchy relation in cubic metals." *Scripta Metallurgica*, 5(9), 787–790.
- Topin, V., Delenne, J.-Y., Radjaï, F., Brendel, L., and Mabilbe, F. (2007). "Strength and failure of cemented granular matter." *Eur. Phys. J. E*, 23(4), 413–429.
- van Mier, J. G. M. (2007). "Multi-scale interaction potentials (F-r) for describing fracture of brittle disordered materials like cement and concrete." *Int. J. Fract.*, 143(1), 41–78.
- Zhao, G.-F., Fang, J., and Zhao, J. (2011). "A 3D distinct lattice spring model for elasticity and dynamic failure." *Int. J. Numer. Anal. Methods Geomech.*, 35(8), 859–885.